RSC Advances

PAPER

View Article Online
View Journal | View Issue

Cite this: *RSC Adv.*, 2025, **15**, 22789

Detection of lamivudine using liquid-surface-enhanced Raman spectroscopy†

Lebogang Thobakgale, *[a] Lungile Nomcebo Thwala[a] and Patience Mthunzi-Kufa[ab]

Antiretroviral medications such as lamivudine (LAM) are central to the treatment of HIV/AIDS. Because of the rise in the substandard production of these pharmaceuticals, new methods of quality control are required. In this study, the use of silver nanoparticles (AgNPs) for the detection and quantification of LAM at low concentrations was explored using a new method known as liquid-surface enhanced Raman spectroscopy (liquid-SERS). AgNPs (20–80% v/v) were prepared by chemical reduction and subsequently characterized by assessing their size, shape, absorbance, and molecular properties. A series of LAM samples (0–80 μg ml^{-1}) were then spiked with AgNPs and evaluated using liquid-SERS. Subsequently, a partial least-square analysis was conducted to determine the linearity (R^2), sensitivity, limit of detection (LOD) and quantification (LOQ) of selected peak ratios. The results show an improved sensitivity for the 783 cm^{-1} band of the drug when coupled with the 945 cm^{-1} band of the citrate stabilizer, which is likely facilitated by intermolecular forces such hydrogen bonding dipole–dipole forces between the functional groups. Secondly, the R^2 ranged between 0.96–0.98, while the LOD and LOQ reached 1.12 to 10.49 and 3.39 to 31.77 μg ml^{-1} respectively. These values were found to be comparative to results reported using common techniques such as UV-vis spectroscopy and high-performance liquid chromatography. As such, it was concluded that further investigation into drug/AgNPs and liquid-SERS could provide new methods of quality control of pharmaceutical products at low concentrations, through a rapid, complementary and cost-effective photonics approach.

Received 14th April 2025
Accepted 24th June 2025

DOI: 10.1039/d5ra02614h

rsc.li/rsc-advances

1 Introduction

The World Health Organization (WHO) monitors the global response to the HIV/AIDS pandemic and the national antiretroviral (ART) programs that aim to provide medication to affected citizens. In the latest WHO report, concerns have been raised over the increased production and distribution of falsified medication, their impact on health systems, challenges in regulatory systems and supply chain complexities.[1] Furthermore, preventive steps to detect and catalogue substandard medication are now a major area of focus for the organization, which means improved scientific methods for quality control of pharmaceutical products have become an urgent priority.[2]

The current pharmacopeia approved scientific methods used for quality control of medication have been instrumental in profiling various chemical aspects of pharmaceutical products. Such techniques include (but are not limited to) high-performance liquid chromatography (HPLC), mass spectrometry (MS) and UV-vis spectroscopy (UV), which are often coupled together for simultaneous separation and detection applications. For example, HPLC-UV allows separation and detection of active pharmaceutical ingredients with high specificity and sensitivity where studies using this technique have reported limits of detection and quantification (LOD and LOQ) of ARV lamivudine at 0.32 and 1.06 μg ml^{-1} respectively,[3] while another reported even lower values of 0.1 and 0.32 μg ml^{-1}.[4] Similarly, MS research published detection of LAM in plasma at a concentration between 10 and 50 μg ml^{-1} using liquid chromatography for separation of solutes (LC-MS).[5] Another study on HPLC-UV published LOD and LOQ values for lamivudine tablets at 0.58 and 1.75 μg ml^{-1}.[6] It is evident that these techniques offer analysis of single molecules at low concentrations, which can be applied to substandard medication. However, there are a few known disadvantages of these techniques that limit their versatility and real-time application. Firstly, HPLC is a complex and expensive method, which may lack sensitivity to compounds that elude at the same time. Secondly, method optimization, sample preparation and the lack of a single detector for analysis of all the chemicals makes it time-consuming.[7] Thirdly, MS is an expensive, sample destructive method which is only accurate for pure samples, therefore it is dependent on chromatography.[8,9] It is therefore worthwhile assisting these techniques by researching new methods that require less effort, time and finance, while yielding similar or better results.

[a]*Photonics Centre, Council for Scientific and Industrial Research, PO Box 395, Pretoria, 0001, South Africa. E-mail: LThobakgale@csir.co.za*

[b]*School of Interdisciplinary Research and Graduate Studies (UNESCO), College of Graduate Studies, University of South Africa, Preller Street, Muckleneuk Ridge, Pretoria, South Africa*

† Electronic supplementary information (ESI) available. See DOI: https://doi.org/10.1039/d5ra02614h

Raman spectroscopy is an optical, label-free modality widely utilized for drug analysis due to its rapid ability to provide detailed molecular vibrational information. However, conventional Raman spectroscopy suffers from inherently weak signal intensity, necessitating high laser power and long integration times for effective detection. This limitation results in a relatively slow and inefficient analytical process. Surface-enhanced Raman spectroscopy (SERS) addresses these shortcomings by significantly amplifying the Raman signal through the use of plasmonic nanostructures.[10] SERS offers several advantages, including non-destructive analysis, specific fingerprint spectra, high sensitivity, low sample consumption, simple operation, and low ongoing costs. The enhancement effect in SERS enables the detection of trace levels of analytes, thereby overcoming the sensitivity limitations of traditional Raman spectroscopy.[11,12]

In SERS, when molecules are adsorbed onto nano-roughened noble metal surfaces such as silver (Ag), gold (Au), or copper (Cu), the Raman signal is substantially amplified. These plasmonic nanoparticles exhibit strong surface plasmon resonance (SPR) in the visible to near-infrared range, generating a localized SPR (LSPR) effect that can theoretically enhance Raman signals by up to 10^{14}-fold, making single-molecule detection feasible.[13] SERS also provides highly specific spectral fingerprints, enabling the differentiation of drugs within complex biological matrices. This feature reduces interference and enhances selectivity in analytical applications.[14]

SERS techniques are typically categorized into two types: solid and liquid SERS. Solid SERS substrates generally offer stronger signal enhancement than metal colloids. However, they are limited by issues such as fixed analyte distribution within the laser focus area, and potential complications like photobleaching, combustion, sublimation, or photocatalysis due to constrained laser energy and sample density.[11] In contrast, liquid SERS employs a solution of nanoparticles without embedding them in a solid substrate, simplifying the preparation process and eliminating the need for drying steps. Colloidal silver and gold nanoparticles, typically ranging from 10 to 150 nm in size, are the most commonly used SERS-active materials due to their pronounced SPR effects in the visible and near-infrared ranges.[15,16]

Several studies highlight the effectiveness of colloidal SERS in drug detection. For instance, Berg *et al.* utilized silver colloids synthesized by reducing silver nitrate with hydroxylamine to distinguish between the SERS and normal Raman spectra of amphetamine and amphetamine-H^+. Similarly, Alharbi *et al.* detected tramadol in water and artificial urine using a silver hydroxylamine colloidal solution, achieving limits of detection of 5.0×10^{-4} M and 2.5×10^{-6} M, respectively.[17,18] Alder *et al.* demonstrated the detection of freebase cocaine using a colloidal silver-based SERS substrate.[19]

In this study, we offer the use of nano-chemistry and liquid surface-enhanced Raman spectroscopy (liquid-SERS).[20–22] This approach employs the advantages of silver nanoparticles (AgNPs) for signal enhancement applications *via* their plasmonic properties, to improve the sensitivity of the technique.[23,24] The AgNPs offer molecular functional groups from the stabilizer, which can interact with the analyte *via* intermolecular forces (hydrogen bonding, polar, dipole–dipole, π–π, *etc*).[25–27] These interactions alter the polarizability, tensile stress, crystallinity, and concentration of the functional groups of the analytes, which allows detection of changes in chemical properties both qualitatively and quantitatively.[28,29] AgNPs are excellent choices for SERS due to their ability to generate strong electromagnetic fields, ease of preparation, broad wavelength response, and versatility for creating specific SERS tags. The ability to enhance the Raman signal in the electromagnetic field (EM) of silver is 2–3 times higher than that of gold. This is because its band gap d–s is in the UV region, causing less damping of the plasmon mode.[13]

Herein, citrate-stabilized silver nanoparticles (AgNPs) were synthesized using chemical reduction method and subsequently characterized using transmission electron microscopy (TEM) (shape and size), dynamic light scattering (DLS) (size), UV-vis spectroscopy and Raman spectroscopy for optical and molecular analysis, respectively. Lamivudine was analyzed at low concentrations with and without the AgNPs for comparison. Lastly, validation parameters such as linearity, limit of detection, and limit of quantification were studied using partial least square analysis. The study is unique because experiments on lamivudine using RS are mostly reported from a computational perspective, leaving room to explore the experimental applications, especially using liquid-SERS.

2 Materials and methods

2.1 Synthesis of citrate stabilized silver nanoparticles

Silver citrate nanoparticles were synthesized using a revised version of the Lee and Meisel method.[30,31] Briefly, 22.5 mg of silver nitrate ($AgNO_3$, Sigma: 101510) was dissolved in 125 ml of deionized water and brought to a boil. 12.5 ml of 1% (v/v) sodium citrate solution was pipetted into the boiling solution and stirred for 1 hour. The solution turned yellow green which indicated the presence of silver nanoparticles. A serial dilution of 0–100% nanoparticle solutions was prepared using deionized water and subsequently analyzed.

2.2 Characterization of silver nanoparticles

2.2.1 Physicochemical properties of AgNPs. The average hydrodynamic diameter and polydispersity index (PDI) of the NCs were determined by dynamic light scattering (DLS) whilst the zeta potential (surface charge) was calculated from the electrophoretic mobility values determined by laser doppler anemometry (LDA) both measured by a Zetasizer® Nano-ZS, ZEN 3600, Malvern instruments, (Worcestershire, UK) equipped with a red laser light beam ($\lambda = 632.8$ nm). For particle size and PDI measurements, the NPs were diluted 50× in milliQ water and for ζ-potential they were diluted 50× in 1 mM KCl.

2.2.2 Morphological properties of AgNPs. The high-resolution transmission electron microscope (HR-TEM, Joel JEM 2100) was used to analyze the shape and surface morphology of the NPs. A drop of stock AgNPs was deposited on a copper grid, washed 3× with Milli-Q water, allowed to dry, and then viewed under TEM. Analysis was conducted using a focal

length of 2.7 mm, 1500× magnification, and a resolution of 0.5 nm. Images were further processed using ImageJ to determine nanoparticle morphology.

2.2.3 UV-vis spectroscopy. Nanoparticle solutions of 0, 20, 40, 60, 80 and 100% concentrations were prepared using deionized water. 2 μL of each solution was pipetted onto a Thermofischer Nanodrop 2000 spectrometer and spectra were collected from an average of three measurements. The spectral data was processed using Microsoft Excel to determine absorption wavelength, concentration, and nanoparticle size.

2.3 Preparation and analysis of LAM/AgNPs using liquid-SERS

Lamivudine powder (99%) was obtained with gratitude from Aurogen Pharmaceuticals. 1 mg of the sample was weighed and transferred into a tube containing 1 ml of deionized water to make a 1 mg per ml solution. A serial dilution of 0, 20, 40, 60 and 80 μg ml^{-1} was prepared using deionized water and the solutions were spiked 1 in 10 with silver nanoparticle solutions. Control samples were prepared in the absence of nanoparticles. The samples were subsequently analyzed using Raman spectroscopy. Spectral data for lamivudine and AgNPs nanoparticles were acquired using a Horiba LabRam Soleil Raman Microscope equipped with a 532 nm laser and a 10× objective lens. An average of ten spectra per sample was obtained using a 10 mW laser power, 200 μm slid width and 20 seconds acquisition time per scan. Twenty measurements of the blank sample (AgNPs) were taken to assess variability due to instrument noise.

Statistical evaluation of the data was conducted by calculating the standard deviations (SD) of twenty measurements of the blank (σ_{blank}) within the regions of interest using the following equation:

$$\sigma_{(blank)} = \sqrt{[(\sum(x-\mu)^2)/(n-1)]} \quad (1)$$

where x, μ and n are the data points, average and number of measurements respectively. Secondly, the limits of detection (LOD) and limits of quantification (LOQ) from the PLS analysis above were then calculated using the $\sigma_{(blank)}$ from above and the slopes (S) in Fig. 4 by applying the following equations.

$$LOD = 3.3 \times \sigma_{(blank)}/S \quad (2)$$

and

$$LOQ = 10 \times \sigma_{(blank)}/S \quad (3)$$

Lastly, propagation errors of the peak ratios (σ_{ratio}) were also evaluated to measure the precision and/or uncertainty of the method using eqn (4) below.

$$\sigma_{(ratio)} = \sqrt{[(\sigma_{(blank)1}/\text{peak 1})^2 + (\sigma_{(blank)2}/\text{peak 2})^2} \times \text{peak 1/peak 2} \quad (4)$$

The data was processed using LabSpec 6 and Microsoft Excel was used to perform linear regression and quantitative analysis of R^2, sensitivity, LOD, LOQ and statistical errors.

3 Results and discussion

Silver nanoparticles stand out among the most metallic NPs because of their remarkable electrical, optical, thermal, and biological properties. The optical, thermal, and catalytic properties of silver nanoparticles are strongly influenced by their size and shape. In this work, AgNPs were synthesized using the chemical reduction method where silver ions were derived from the silver nitrate salt, and the reducing agent, sodium citrate reduced the ions to atoms and finally, the atoms nucleated and grew into particles.[32]

3.1 Silver nanoparticle morphology, size, and surface charge by TEM and DLS

The average hydrodynamic size of the AgNPs determined using DLS, and UV was found to be in a range of 60 to 70 nm. Whilst surface charge (ζ-potential) analysis showed that the AgNPs are negatively charged at -30.7 ± 7.2 mV ($n = 3$). Microscopy analysis by TEM showed that the AgNPs are spherical in shape with a homogenous size distribution as depicted in Fig. 1 below.

In the next section, the molecular properties of nanoparticles such as size, absorption, chemical functional groups and intermolecular forces are evaluated using UV-vis and Raman spectroscopy techniques.

3.2 UV-vis and Raman spectroscopy of silver nanoparticles

UV-vis spectroscopy was used to confirm the presence of silver nanoparticles, size and concentration using simulated data of the Mie scattering theory and molar extinction coefficients respectively.[33,34] Raman spectroscopy analysis produced data on chemical functional groups at different concentrations, which were used to assess changes in intermolecular forces with citrate. Fig. 2 below shows the spectral data of samples that were prepared as explained in Section 2.2.

The UV-vis spectral data in Fig. 2A above displays an absorbance band at 436 nm with the undiluted (100%) sample showing maximum absorption. Secondly, a slight redshift towards higher wave numbers was observed as concentration increased. This was attributed to changes in intermolecular forces *i.e.* hydrogen bonding, as the concentration changes.[35,36] The Mie scattering model for citrate stabilized silver nanoparticles obtained from literature was used to determine the molar extinction coefficient to be 739 $\times 10^8$ M^{-1} cm^{-1} , this implies the size of the nanoparticles is approximately 60 nm,[37] which is slightly lower than the 70 nm obtained from the DLS experiment in Section 3.1. The difference is attributed to the effects of concentration and refractive index of the media which tends to distort the actual size of the nanoparticle in DLS. Lastly, the Beer–Lambert law equation was used to calculate the actual concentrations of the nanoparticles which ranged between 6.6×10^{11} to 2.52×10^{12} nanoparticles per ml.

Raman spectroscopy experiments revealed key differences that were worth noting. By comparison with pure citrate (1% v/v), the nanoparticle group contained two distinct Raman bands at 150 cm^{-1} and 216 cm^{-1} that are absent in the former. These peaks are significant because they arise from the metal–oxygen

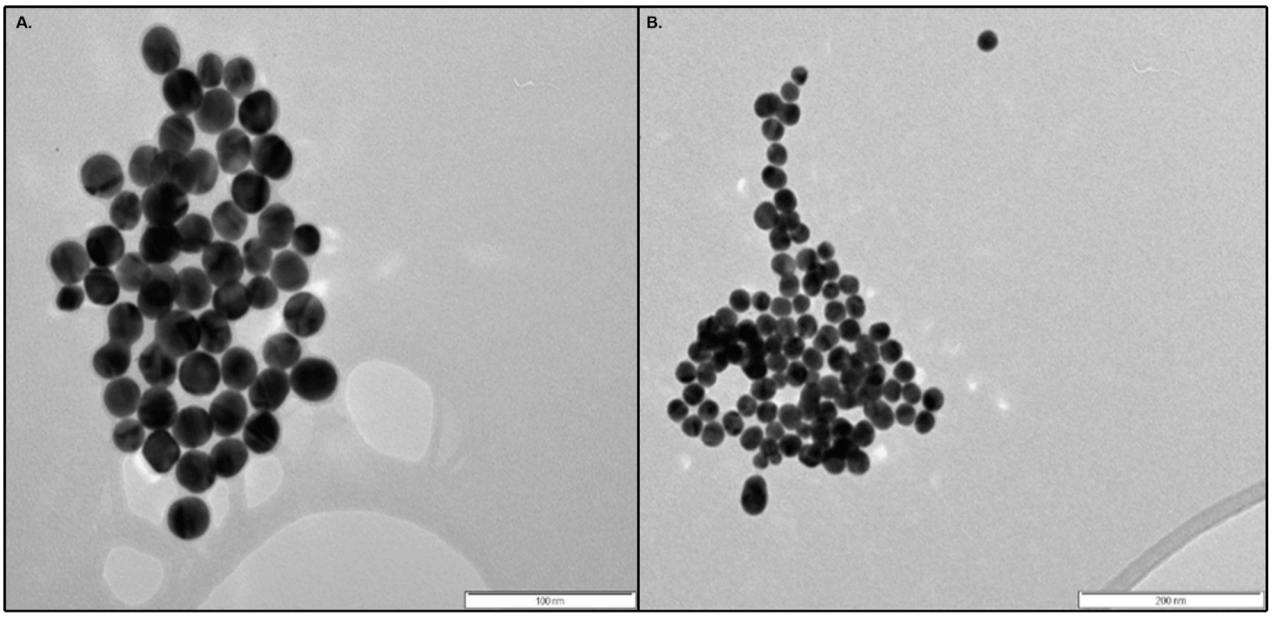

Fig. 1 HR-TEM images of AgNPs. (A) 50 000×; (B) 10 000× magnification. Data on interplanar spacing is provided in the ESI.†

bond that forms during nanoparticle synthesis.[38–40] Also, the bands increase in intensity and redshift towards lower wavenumbers when the concentration increases, similar to the UV-vis data. Broad peaks appear at 396 cm^{-1} and 330 cm^{-1} belonging to aliphatic bonds were detected for the citrate and the nanoparticles respectively.[41] The difference in peak position is assumed to result from increased polarizability when electron density is shared between the hydroxyl, carboxylic and the metal–oxygen bond.[42] New bands such as the weak bending (544 cm^{-1}) [43] and out-of-plane bending (641 cm^{-1}) [44] of carboxylic acid functional groups emerged in the nanoparticle's spectrum, which indicates improved sensitivity towards citrate molecules, induced by increased molecular interactions and possibly plasmonic effects. The aliphatic bond (CC) stretching at 836 cm^{-1} formed a doublet peak at 794 cm^{-1} and 825 cm^{-1}, although the reason for the shape of the peak is unclear, the red-shift further supports the observation in the 300 cm^{-1} region explained above. Another doublet formed from the alpha

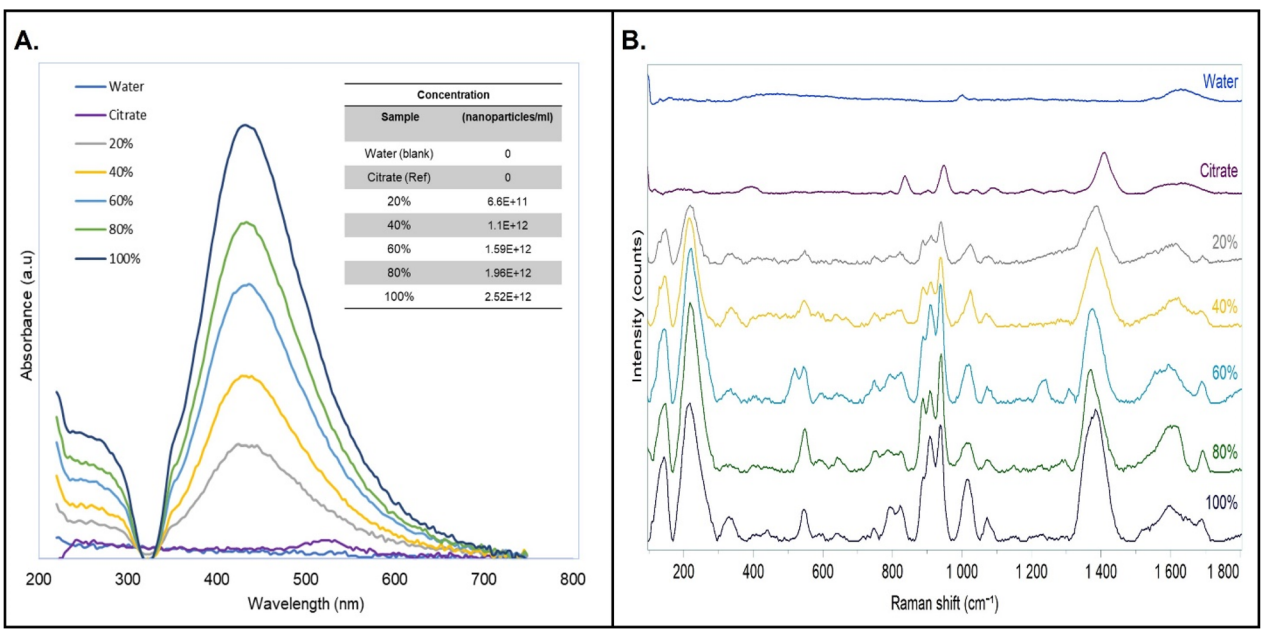

Fig. 2 Qualitative analysis of AgNPs, 0–100% (v/v). (A). UV-vis spectroscopy. (B) Raman spectroscopy. Nanoparticle concentrations by Mie theory calculations (inset).

bond (CCOO) stretching mode, accompanied by a red-shift from 949 cm^{-1} to 909 cm^{-1} and 936 cm^{-1},[44] this implies increased bond deformation and tensile stress, while the increased intensity and bandwidth depicts changes in crystallinity. Low-intensity hydroxyl stretching modes appeared at 1044 cm^{-1} and 1089 cm^{-1} for the citrate spectra and subsequently increased in intensity and red-shifted to 1019 cm^{-1} and 1070 cm^{-1} respectively on the nanoparticles.[43] This observation supports the increased Raman sensitivity towards citrate, facilitated by the nanoparticles, as was the case with the carboxylic groups. Lastly, a strong and narrow band was detected at 1408 cm^{-1} and assigned to the symmetrical stretch of the carboxylic functional group, succeeded by its asymmetrical stretching mode at 1627 cm^{-1}.[45] The former peak increased in bandwidth and red-shifted to 1384 cm^{-1}, further signaling increased bond deformation, tensile stress and crystallinity due to molecular interactions such as hydrogen bonding, dipole–dipole and ionic interactions.[46] Overall, the UV-vis and Raman spectra confirmed the presence of silver nanoparticles by detecting their characteristic absorption band while the latter showed the presence of metal-oxide bonds and all the functional groups belonging to citrate. Lastly, both techniques show an increased intensity and red-shift pattern with increased concentration. The differences in the Raman spectra of the two groups are summarized in Table 1 below.

Table 1 Raman bands (cm^{-1}) of citrate (1% v/v) and citrate stabilized silver nanoparticles (AgNPs)[43–45,47a]

Water	Citrate	AgNPs	Assignment
—	—	150	ν_s (metal–O)
—	—	216	ν_s (metal–O)
	396	330	ν_s (CC)
—	—	544	ν_s (COO)
—	—	641	$\delta_{out\text{-}plane}$ (COO)
—	836	794, 822	ν_s (CC)
—	949	909, 936	ν_s (C–COO)
1003	—	—	ν_s (CC)
—	1044, 1089	1019, 1070	ν_s (COH)
—	1408	1384	ν_s (COO)
1631	1627	1596, 1692	ν_s (C=O), ν_s (COO), ν_s (HOH)

[a] ν_s, symmetric stretch; ν_a, asymmetric stretch; $\delta_{out\text{-}plane}$, bending.

Given the observed characteristics and considering potential saturation of the analyte Raman signal, the 60% AgNPs containing 1.59×10^{12} nanoparticles per ml was chosen for detection and analysis of lamivudine using liquid-enhanced Raman spectroscopy (Fig. 3).

3.3 Characterization of lamivudine using liquid enhanced Raman spectroscopy

Lamivudine was studied at low concentrations (0–80 μg ml^{-1}) to determine the signal enhancement capabilities of AgNPs. Fig. 4 below depicts the Raman spectra (500–1800 cm^{-1}) of the drug at 80 μg ml^{-1} without nanoparticles, followed by a serial dilution of the drug in the presence of AgNPs.

From top to bottom, the results show two significant peaks from the drug at 1003 cm^{-1} and 1624 cm^{-1}, which were assigned to the aromatic breathing mode from the polystyrene plate and stretching mode of water, respectively.[48,49] When compared to the drug/nanoparticle series, significant peaks were observed, beginning with 549 cm^{-1} and 592 cm^{-1} of the citrate carboxylic acid (stretching mode) and a twisting mode of the lamivudine respectively. In the former case, the band is blue shifted compared to the nanoparticles (pink), which implies a change in intermolecular forces. Ring deformation of R_2 appeared twice, at 692 cm^{-1} (weak) followed by a strong sharp signal at 783 cm^{-1}.[50–52] Peaks 946 cm^{-1}, 1026 cm^{-1} and 1074 cm^{-1} of the citrate functional groups also blue-shifted, indicating an observable change in molecular interactions caused by chemical bonding. Ring 2 vibrations were detected at 1192 cm^{-1}, succeeded by a strong mixture of bending and

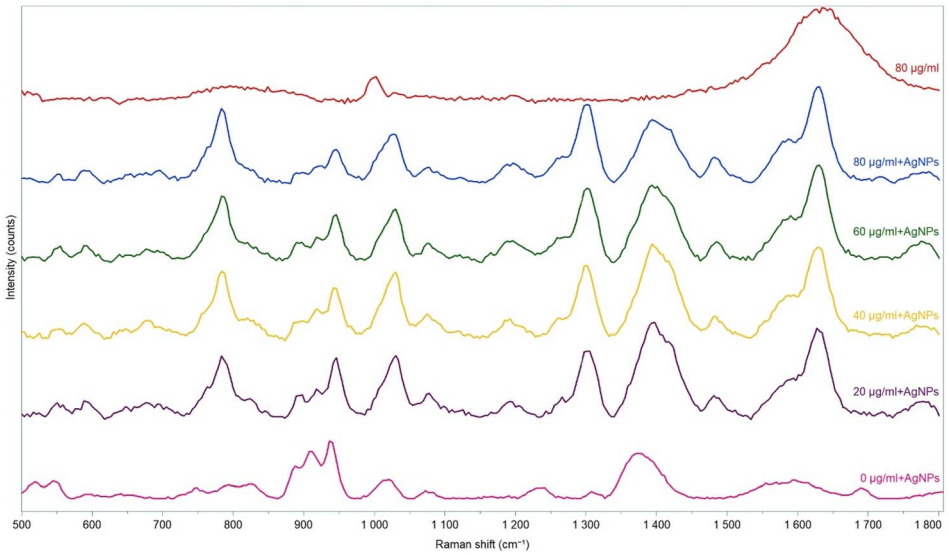

Fig. 3 Raman spectroscopy of lamivudine (0–80 μg ml^{-1}) in the presence of AgNPs.

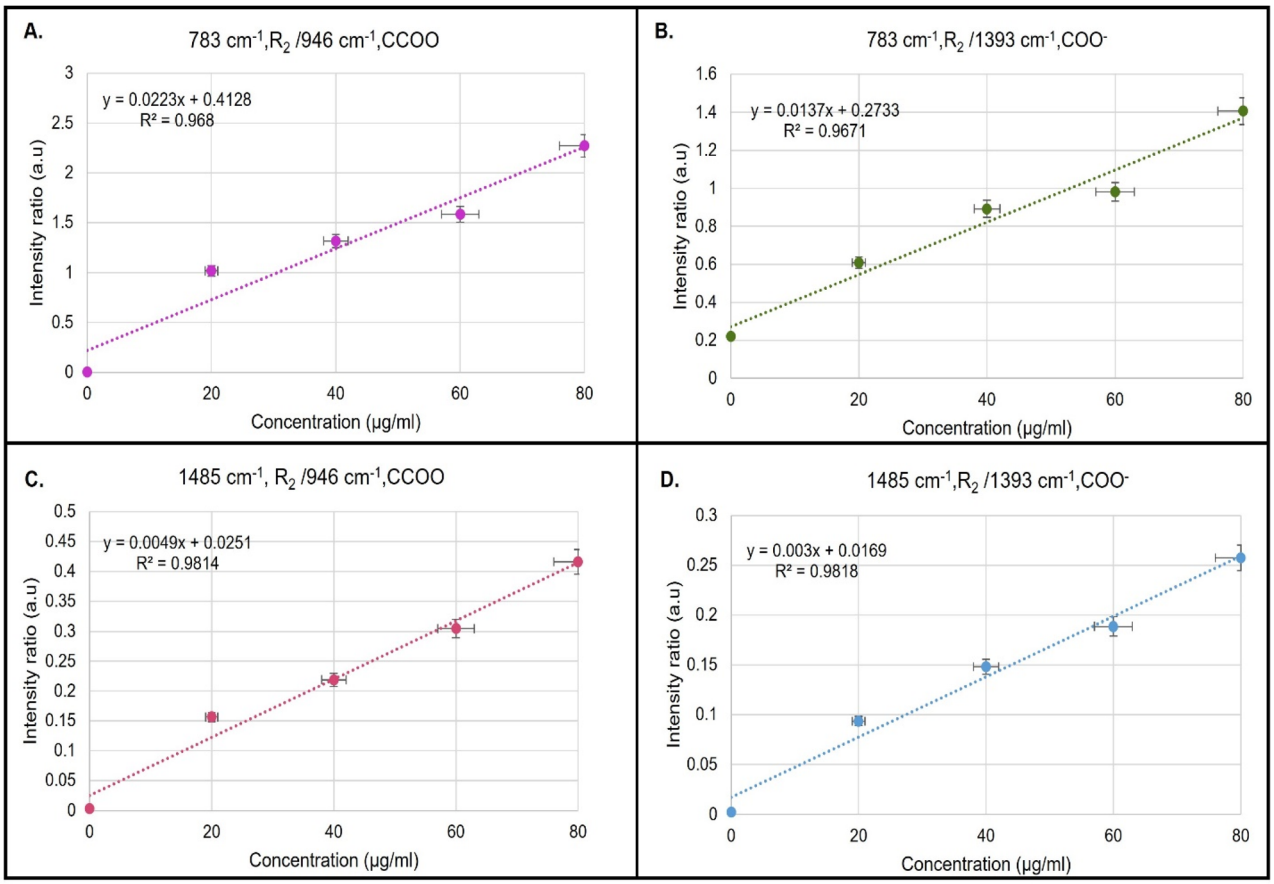

Fig. 4 PLS from peak ratios of lamivudine and AgNPs. (A) 783 cm^{-1}/946 cm^{-1}; (B) 783 cm^{-1}/1393 cm^{-1}; (C) 1485 cm^{-1}/946 cm^{-1}; (D) 1485 cm^{-1}/1393 cm^{-1}.

twisting modes of R_2 at 1301 cm^{-1}.[52] Band broadening of the carboxylic stretching mode of citrate was observed at a blue shifted position of 1393 cm^{-1}, likely caused by reduced crystallinity in response to chemical bonding with the drug. A new peak from aromatic moieties of the drug, likely carbon and nitrogen double from pyrimidine, emerged at 1485 cm^{-1}, indicating improved sensitivity and detection of the drug. Lastly, a strong narrow band from a combination of carbonyl stretching mode and the bending of water appeared at 1627 cm^{-1}, the shape of the peaks implies improved crystallinity contributed by the drug/nanoparticle interaction. Generally, detection of lamivudine was not possible in the absence of nanoparticles, which indicates the limitations of the conventional Raman technique such as low signal detection.[53] When nanoparticles were incorporated, a considerable number of peaks were detected, while the original position of the silver nanoparticle bands shifted to higher wavenumbers. This combination of results confirms molecular interactions between the drug and nanoparticles, which led to improved sensitivity and detection by liquid enhanced Raman spectroscopy.[54,55] A summary of the Raman bands reported on the study is shown in Table 2 below.

From the above spectral data and table, it can be seen that peaks 783 cm^{-1} and 1485 cm^{-1} of R_2 reacted uniquely to the nanoparticles, likely due to hydrogen bonding between their amino and amide groups and the citrate functional groups. As such, peak ratios between the former and the 946 cm^{-1} and 1393 cm^{-1} peaks of citrate were used to evaluate the interaction quantitatively by linear regression methods.

Table 2 Raman bands (cm^{-1}) of lamivudine (0–80 µg ml^{-1}) in the presence of AgNPs.[50–52a]

Water	Lamivudine	Lamivudine/AgNPs	Assignment
—	—	549, 592	τ (skel), ν_s (COO)
—	—	692	Deformation R_2 ring
	—	783	Deformation R_2 ring
—	—	946	ν_s (C–COO)
1002	998	—	Benzene
—	—	1026, 1074	ν_s (C–COO); ν_s (COH)
—	1196	—	ν_s (C–C)
—	—	1192	ν_s (C=C), ν_s (C_4–N)
—	—	1301	τ (R_2)
—	—	1393	ν_s (COO)
—	—	1485	δ (–NH_2), ν_s (COO), ν_s (C=N)
1624	1638	1627	ν_s (C=O), ν_s (COO), δ (OH)

[a] ν_s symmetric stretch; ν_a, asymmetric stretch; $\delta_{out\text{-}plane}$, bending, τ; twisting.

Table 3 Results of PLS analysis of drug/AgNPs using liquid SERS

Parameter	783 cm^{-1}/946 cm^{-1}	783 cm^{-1}/1393 cm^{-1}	1485 cm^{-1}/946 cm^{-1}	1485 cm^{-1}/1393 cm^{-1}
Linear range	0–80 (μg ml^{-1})			
Regression equation	$y = 0.0223x + 0.4128$	$y = 0.0137x + 0.2733$	$y = 0.0049x + 0.0251$	$y = 0.003x + 0.0169$
R^2	0.968	0.9671	0.9814	0.9818
Sensitivity (S)	0.0223	0.0137	0.0049	0.003
Limit of detection (LOD)	1.12	1.79	6.42	10.49
Limit of quantification (LOQ) (μg ml^{-1})	3.39	5.44	19.45	31.77
Precision (σ_{ratio})	0.00061	0.00053	0.00062	0.00052

3.4 Partial least square (PLS) analysis of lamivudine/AgNPs

The Raman data from the selected peaks from Section 3.3 were processed into peak ratios and plotted against the drug concentration. As a result, linear graphs were obtained and used to determine key analytic parameters such as R^2, sensitivity, limit of detection and limit of quantification. Fig. 4 below depicts four graphs obtained from the peak ratios, each data point is an average of three measurements, percent error bars are included for each concentration.

The plots shown in Fig. 4 display a linear relationship between the peak intensity ratio and concentration. The R^2 values for Fig. 4A and B were found to be similar at 0.96, while the calibration sensitivity, indicated by the slopes of the equations show a higher value on the former. This indicates that the intensity of the alpha carbon peak decreases faster than the carboxylic acid as the concentration of the drug increases, mostly likely due to an increase in dipole moment and polarizability caused by the pulling of electrons away from the alpha carbon towards the carboxylic carbon. Similarly, Fig. 4C and D have the same R^2 value, while the former shows a higher sensitivity towards the change in concentration, due to the same molecular interaction explained above. When comparing the behavior of the drug in terms of ring 2 vibrations (Fig. 4A and C), a higher R^2 value is observed in the latter, however, the 783 cm^{-1} intensity increased at a higher rate with concentration. Likewise, the R^2 value of peak 1485 cm^{-1} was higher than 783 cm^{-1}, while the latter was more sensitive (Fig. 4B and D). This is expected because the ring deformation mode is more polarized due to the pi-electron delocalization, which would affect the linearity compared to localized electron bonds, while giving a high Raman signal.

Quantitatively, the standard deviation from the blank measurements $\sigma_{(blank)}$ ranged between 0.00086 and 0.0009 for the regions of interest (eqn (1)), indicating a low variation and good stability between measurements. Similarly, the propagation errors of the peak ratios were in the region of 0.0005–0.0006 (eqn (4)), which shows acceptable precision for measuring the selected peaks of interest. Generally, low SD values also imply high reproducibility, however, more experiments using larger sample groups are still required to confirm this aspect. Table 3 below is a summary of the parameters evaluated from the PLS analysis.

An assessment of Table 3 above shows that the LOD and LOQ of peak ratio 783 cm^{-1}/946 cm^{-1} are lower than the 783 cm^{-1}/1393 cm^{-1}, similar to the 1485 cm^{-1}/946 cm^{-1} and 1485 cm^{-1}/1393 cm^{-1} groups. This indicates that the changes in the alpha carbon of the citrates offer better detection of the drug compared to its carboxylic functional group because they are more polarized as explained above. Secondly, when comparing the behavior of 783 cm^{-1}/946 cm^{-1} to 1485 cm^{-1}/946 cm^{-1}, the former ratio shows higher values of LOD and LOQ, because of the combination of ring deformation and the more reactive alpha carbon. Thirdly, peak ratios 783 cm^{-1}/1393 cm^{-1} and 1485 cm^{-1}/1393 cm^{-1} also support the previous observation where, the more Raman reactive ring deformation shows better detection and quantification than its individual bonds. Lastly, the overall detection limit across all the ratios was between 1.12–10.49 μg ml^{-1}, while the limit of quantitation ranged between 3.39 and 31.77 μg ml^{-1}. These values are significant because they are comparable to data published using standard methods such as UV-vis spectroscopy and HPLC. As such, the results in the study show the capability of AgNPs in the improvement of detection of lamivudine at low concentrations, which is essential in method development for drug analysis using Raman spectroscopy.

4 Conclusion

In summary, the experiments conducted in this study included the synthesis and characterization of citrate stabilized silver nanoparticles, followed by experiments on lamivudine at low concentrations using liquid-surface enhanced Raman spectroscopy (liquid-SERS). The aim was to assess the applicability of the nanoparticles for detection of the drug for quality control. Differences in peak intensity ratios revealed a trend where the citrate signals decrease significantly when the ring deformation of the drug was analyzed, compared to the individual bonds on the ring. The results showed that signal improvement was achieved through the intermolecular forces between the drug and citrate molecules as well as plasmonic effects from the silver metal. PLS analysis produced R^2 and sensitivity values (LOD and LOQ) comparable to conventional methods, which implies the liquid-SERS method can be used complementary to these techniques, for the purpose of quality control of pharmaceutical products. Future work will entail developing a full method according to ICH guidelines and applying the technique to known substandard medication.

Data availability

The data supporting this article have been included as part of the ESI.†

Author contributions

L. T. and L. T. conducted all of the experimental work. L. T. compiled and processed the data to compile the manuscript, while L. T. reviewed the analysis and manuscript and designed the graphical abstract. P. M. K provided the facilities and funding support. All authors have read and agreed to the published version of the manuscript.

Conflicts of interest

There are no conflicts to declare.

Acknowledgements

The authors acknowledge the financial support received from the Council for Scientific and Industrial Research (CSIR), National Research Fund (NRF), and Department of Science and Innovation (DSI).

References

1 WHO, *World health statistics 2024: monitoring health for the SDGs, sustainable development goals*, World Health Organization, 2024.
2 Global Surveillance and Monitoring System for substandard and falsified medical products. 2017. Available: https://www.iris.who.int/.
3 T. M. Dezani, A. B. Dezani and C. H. D. R. Serra, Development and validation of rp-hplc method for simultaneous determination of lamivudine, stavudine, and zidovudine in perfusate samples: Application to the single-pass intestinal perfusion (spip) studies, *Braz. J. Pharm. Sci.*, 2021, **57**, 1–12, DOI: 10.1590/S2175-97902020000419073.
4 V. S. Adhao, *et al.*, Reverse phase-liquid chromatography assisted protocol for simultaneous determination of lamivudine and tenofovir disoproxil fumarate in combined medication used to control HIV infection: an investigative approach, *Futur J. Pharm. Sci.*, 2021, **7**(1), DOI: 10.1186/s43094-021-00233-3.
5 A. Shelke, T. Lokhande and V. Pardeshi, Sensitive Quantification of Antiretroviral Trio in Plasma: Lamivudine, Zidovudine, and Nevirapine by LC-MS/MS with Abacavir, *Int. J. Pharm. Qual. Assur.*, 2024, **15**(1), 357–365, DOI: 10.25258/ijpqa.15.1.57.
6 K. Somkuwar, P. Sabale, V. Sawale and P. Rahangdale, Comparative study of UV spectroscopy, RP-HPLC and HPTLC methods for quantification of antiviral drug lamivudine in tablet formulation, *Futur J. Pharm. Sci.*, 2024, **10**(1), DOI: 10.1186/s43094-024-00651-z.
7 Y. L. Chew, M. A. Khor and Y. Y. Lim, Choices of chromatographic methods as stability indicating assays for pharmaceutical products: A review, *Heliyon*, 2021, **7**(3), e06553, DOI: 10.1016/J.HELIYON.2021.E06553.
8 G. Kaklamanos, E. Aprea, and G. Theodoridis, Mass Spectrometry: Principles and Instrumentation, *Encyclopedia of Food and Health*, 2015, pp. 661–668, DOI: 10.1016/B978-0-12-384947-2.00447-5.
9 A. L. Rockwood, M. M. Kushnir, and N. J. Clarke, Mass Spectrometry, *Principles and Applications of Clinical Mass Spectrometry: Small Molecules, Peptides, and Pathogens*, 2018, pp. 33–65, DOI: 10.1016/B978-0-12-816063-3.00002-5.
10 T. Yin, Y. Peng, K. Chao and Y. Li, Emerging trends in SERS-based veterinary drug detection: multifunctional substrates and intelligent data approaches, *npj Sci. Food*, 2025, **9**(1), 1–21, DOI: 10.1038/s41538-025-00393-z.
11 E. Bickerstaff-Westbrook, A. Tukova, N. Lyu, C. Shen, A. Rodger and Y. Wang, Advancing SERS label-free detection of bacteria: Sensing in liquid *vs.* drop-cast, *Mater. Today Sustain.*, 2024, **27**, 100912, DOI: 10.1016/J.MTSUST.2024.100912.
12 C. Liu, *et al.*, Toward SERS-based therapeutic drug monitoring in clinical settings: Recent developments and trends, *TrAC, Trends Anal. Chem.*, 2023, **164**, DOI: 10.1016/J.TRAC.2023.117094.
13 H. Lai, X. Wang, M. Qi, H. Huang and B. Yu, Advances in Surface-Enhanced Raman Spectroscopy for Therapeutic Drug Monitoring, *Molecules*, 2025, **30**(1), 15, DOI: 10.3390/MOLECULES30010015.
14 S. S. Panikar, D. Cialla-May, E. De la Rosa, P. Salas and J. Popp, Towards translation of surface-enhanced Raman spectroscopy (SERS) to clinical practice: Progress and trends, *TrAC, Trends Anal. Chem.*, 2021, **134**, DOI: 10.1016/J.TRAC.2020.116122.
15 S. Azimi and A. Docoslis, Recent Advances in the Use of Surface-Enhanced Raman Scattering for Illicit Drug Detection, *Sensors*, 2022, **22**(10), 3877, DOI: 10.3390/S22103877.
16 H. Kearns, R. Goodacre, L. E. Jamieson, D. Graham and K. Faulds, SERS Detection of Multiple Antimicrobial-Resistant Pathogens Using Nanosensors, *Anal. Chem.*, 2017, **89**(23), 12666–12673, DOI: 10.1021/ACS.ANALCHEM.7B02653.
17 R. W. Berg, T. Nrbygaard, P. C. White and S. Abdali, Ab initio calculations and Raman and SERS spectral analyses of amphetamine species, *Appl. Spectrosc. Rev.*, 2011, **46**(2), 107–131, DOI: 10.1080/05704928.2010.520180.
18 O. Alharbi, Y. Xu and R. Goodacre, Detection and quantification of the opioid tramadol in urine using surface enhanced Raman scattering, *Analyst*, 2015, **140**(17), 5965–5970, DOI: 10.1039/c5an01177a.
19 R. Alder, *et al.*, Application of plasma-printed paper-based SERS substrate for cocaine detection, *Sensors*, 2021, **21**(3), 1–13, DOI: 10.3390/s21030810.
20 L. Tian, *et al.*, Liquid-state quantitative SERS analyzer on self-ordered metal liquid-like plasmonic arrays, *Nat. Commun.*, 2018, **9**(1), DOI: 10.1038/s41467-018-05920-z.
21 X. Xu, *et al.*, Dynamic liquid surface enhanced Raman scattering platform based on soft tubular microfluidics for label-free cell detection, *Anal. Chem.*, 2019, **91**(13), 7973–7979, DOI: 10.1021/acs.analchem.9b01111.
22 Z. Ji, *et al.*, Magnetically Enhanced Liquid SERS for Ultrasensitive Analysis of Bacterial and SARS-CoV-2

Biomarkers, *Front. Bioeng. Biotechnol.*, 2021, **9**, DOI: 10.3389/fbioe.2021.735711.

23 X. Wang, *et al.*, Hybrid surface plasmon effect and SERS characterization in a heterogeneous composite structure of Au nano-array and Ag film, *Results Phys.*, 2020, **17**, DOI: 10.1016/j.rinp.2020.103175.

24 L. Thobakgale, S. Ombinda-Lemboumba and P. Mthunzi-Kufa, Chemical Sensor Nanotechnology in Pharmaceutical Drug Research, *Nanomaterials*, 2022, **12**(15), DOI: 10.3390/nano12152688.

25 J. M. C. Marques, F. V. Prudente, and F. Pirani, *Intermolecular Forces: from Atoms and Molecules to Nanostructures*, MDPI, 2022, DOI: 10.3390/molecules27103072.

26 Z. Yu and R. R. Frontiera, Intermolecular Forces Dictate Vibrational Energy Transfer in Plasmonic-Molecule Systems, *ACS Nano*, 2022, **16**(1), 847–854, DOI: 10.1021/acsnano.1c08431.

27 Z. Chu, Y. Han, P. Král and R. Klajn, Precipitation on Nanoparticles': Attractive Intermolecular Interactions Stabilize Specific Ligand Ratios on the Surfaces of Nanoparticles, *Angew. Chem.*, 2018, **130**(24), 7141–7145, DOI: 10.1002/ange.201800673.

28 A. Bhaumik, A. M. Shearin, R. Delong, A. Wanekaya and K. Ghosh, Probing the interaction at the nano-bio interface using Raman spectroscopy: ZnO nanoparticles and adenosine triphosphate biomolecules, *J. Phys. Chem. C*, 2014, **118**(32), 18631–18639, DOI: 10.1021/jp506200a.

29 H. S. Bahlol, J. Li, J. Deng, M. F. Foda and H. Han, Recent Progress in Nanomaterial-Based Surface-Enhanced Raman Spectroscopy for Food Safety Detection, *Nanomaterials*, 2024, **14**(21), 1750, DOI: 10.3390/nano14211750.

30 B. Dong, *et al.*, Synthesis of monodisperse spherical AgNPs by ultrasound-intensified Lee-Meisel method, and quick evaluation *via* machine learning, *Ultrason. Sonochem.*, 2021, **73**, 105485, DOI: 10.1016/J.ULTSONCH.2021.105485.

31 U. T. Khatoon, G. V. S. N. Rao, K. M. Mantravadi, and Y. Oztekin, *Strategies to Synthesize Various Nanostructures of Silver and Their Applications – A Review*, Royal Society of Chemistry, 2018. DOI: 10.1039/c8ra00440d.

32 I. Ivanov, *et al.*, Synthesis of Silver Nanoparticles: From Conventional to 'Modern' Methods—A Review, *Processes*, 2023, **11**(9), 2617, DOI: 10.3390/PR11092617.

33 E. G. Wrigglesworth and J. H. Johnston, Mie theory and the dichroic effect for spherical gold nanoparticles: an experimental approach, *Nanoscale Adv.*, 2021, **3**(12), 3530–3536, DOI: 10.1039/d1na00148e.

34 I. Weiner, M. Rust and T. D. Donnelly, Particle size determination: An undergraduate lab in Mie scattering, *Am. J. Phys*, 2001, **69**(2), 129–136, DOI: 10.1119/1.1311785.

35 Hema, *et al.*, Computational study of the intermolecular interactions and their effect on the UV-visible spectra of the ternary liquid mixture of benzene, ethanol and propylene glycol, *J. Mol. Model.*, 2020, **26**(10), DOI: 10.1007/s00894-020-04533-y.

36 S. Yanagisawa, T. Yasuda, K. Inagaki, Y. Morikawa, K. Manseki and S. Yanagida, Intermolecular interaction as the origin of red shifts in absorption spectra of zinc-phthalocyanine from first-principles, *J. Phys. Chem. A*, 2013, **117**(44), 11246–11253, DOI: 10.1021/jp407608w.

37 D. Paramelle, A. Sadovoy, S. Gorelik, P. Free, J. Hobley and D. G. Fernig, A rapid method to estimate the concentration of citrate capped silver nanoparticles from UV-visible light spectra, *Analyst*, 2014, **139**(19), 4855–4861, DOI: 10.1039/c4an00978a.

38 A. C. Sparavigna, Raman Spectroscopy of the Iron Oxides in the Form of Minerals, Particles and Nanoparticles, 2023. DOI: 10.26434/chemrxiv-2023-22kh4-v2.

39 A. J. Kora and J. Arunachalam, Green fabrication of silver nanoparticles by gum tragacanth (astragalus gummifer): A dual functional reductant and stabilizer, *J. Nanomater.*, 2012, **2012**, DOI: 10.1155/2012/869765.

40 A. M. Ondieki, *et al.*, Fabrication of surface-enhanced Raman spectroscopy substrates using silver nanoparticles produced by laser ablation in liquids, *Spectrochim. Acta, Part A*, 2023, **296**, 122694, DOI: 10.1016/J.SAA.2023.122694.

41 S. Pattanayak, A. Swarnkar, A. Priyam and G. M. Bhalerao, Citrate-hydrazine hydrogen-bonding driven single-step synthesis of tunable near-IR plasmonic, anisotropic silver nanocrystals: Implications for SERS spectroscopy of inorganic oxoanions, *Dalton Trans.*, 2014, **43**(31), 11826–11833, DOI: 10.1039/c4dt01091d.

42 S. Menant, *et al.*, Polarisation of electron density and electronic effects: Revisiting the carbon–halogen bonds, *Molecules*, 2021, **26**(20), DOI: 10.3390/molecules26206218.

43 Z. Huang, *et al.*, Quantitative determination of citric acid in seminal plasma by using Raman spectroscopy, *Appl. Spectrosc.*, 2013, **67**(7), 757–760, DOI: 10.1366/12-06902.

44 O. G. Pandoli, *et al.*, Ultra-highly conductive hollow channels guided by a bamboo bio-template for electric and electrochemical devices, *J. Mater. Chem. A*, 2020, **8**(7), 4030–4039, DOI: 10.1039/c9ta13069a.

45 J. Jiang, S. Wang, H. Deng, H. Wu, J. Chen and J. Liao, Rapid and sensitive detection of uranyl ion with citrate-stabilized silver nanoparticles by the surface-enhanced Raman scattering technique, *R. Soc. Open Sci.*, 2018, **5**(11), DOI: 10.1098/rsos.181099.

46 H. S. Samuel, U. Nweke-Maraizu, and E. E. Etim, *Review Article: Understanding Intermolecular and Intramolecular Hydrogen Bonds: Spectroscopic and Computational Approaches*, Sami Publishing Company, 2023, DOI: 10.48309/jcr.2023.407989.1235.

47 H. Wang and H. Wei, Controlled Citrate Oxidation on Gold Nanoparticle Surfaces for Improved Surface-Enhanced Raman Spectroscopic Analysis of Low-Affinity Organic Micropollutants, *Langmuir*, 2022, **38**(16), 4958–4968, DOI: 10.1021/acs.langmuir.2c00367.

48 E. S. Jung, *et al.*, Quantitative Raman analysis of microplastics in water using peak area ratios for concentration determination, *npj Clean Water*, 2024, **7**(1), DOI: 10.1038/s41545-024-00397-4.

49 I. Chakraborty, S. Banik, R. Biswas, T. Yamamoto, H. Noothalapati, and N. Mazumder, *Raman Spectroscopy for*

Microplastic Detection in Water Sources: a Systematic Review, Institute for Ionics, 2023, DOI: 10.1007/s13762-022-04505-0.

50 C. Yuan, *et al.*, High-pressure Polymorphism in Lamivudine, *J. Mol. Struct.*, 2023, **1292**, 136170, DOI: 10.1016/J.MOLSTRUC.2023.136170.

51 B. G. Pereira, *et al.*, Identification of lamivudine conformers by Raman scattering measurements and quantum chemical calculations, *J. Pharm. Biomed. Anal.*, 2007, **43**(5), 1885–1889, DOI: 10.1016/J.JPBA.2007.01.014.

52 Y. Du, *et al.*, Vibrational spectroscopic study of polymorphism and polymorphic transformation of the anti-viral drug lamivudine, *Spectrochim. Acta, Part A*, 2015, **137**, 1158–1163, DOI: 10.1016/j.saa.2014.08.128.

53 M. Deluca, H. Hu, M. N. Popov, J. Spitaler, and T. Dieing, *Advantages and Developments of Raman Spectroscopy for Electroceramics*, Springer Nature, 2023, DOI: 10.1038/s43246-023-00400-4.

54 S. Zhang, W. Chen, H. Shi, W. Zhou and J. Zhang, Theoretical Studies of the Influence of an Intermolecular Force and an Electric Field on the Methanol Raman Spectrum, *J. Phys. Chem. C*, 2020, **124**(13), 6955–6963, DOI: 10.1021/acs.jpcc.9b08736.

55 H. Hushvaktov, L. Djumanov and Sh. Yormatov, Intermolecular interactions in the chloroform solution of methyl-ethyl-ketone: Raman spectroscopy and *ab initio* calculations, *Uzbek J. Phys.*, 2024, **25**(4), DOI: 10.52304/.v25i4.472.